Periodic solar wind forcing due to recurrent Coronal Holes during 1996-2009 and its impact on Earth's geomagnetic and ionospheric properties during extreme solar minimum

S. Tulasi Ram[1], C. H. Liu[2], and S.-Y. Su[3]

[1] Institute of Astronomy and Astrophysics, Academia Sinica, Taipei, Taiwan (R.O.C).

[2] Academia Sinica, Taipei, Taiwan (R.O.C).

[3] Institute of Space Science, National Central University, Chung-li, Taiwan (R.O.C).

Abstract

The periodicities in the area of Coronal Hole (CH) regions on the solar disk and the solar wind (SW) high speed streams (HSS) have been studied, for the first time, during the complete solar cycle 23 (SC 23) from 1996 to 2009 using the solar EUV image data from SOHO, STEREO satellites and ACE solar wind-magnetic data. Both the solar wind velocity and the area of CH regions consistently exhibit large values during the declining phase and the minimum of SC 23 (2003 to 2009) due to equatorward extended holes and/or low-latitude isolated holes. Further, the SW velocity and CH area exhibit greater tendency for sub-harmonic (13.5-day and 9-day) periodicities during the declining phase and solar minimum. The response of Earths' geomagnetic and ionospheric properties to these periodicities associated with Co-rotating Interaction Regions (CIRs) in high speed solar wind streams is studied with focus during the extremely low solar activity period of 2008. The sub-harmonic oscillations in both day and night side ionospheric electron density are found to correlate well with the oscillations in SW and Kp during 2008. The topside ionospheric response (above 350 km) appears to be dominated by the changes in the plasma temperature and/or scale height and exhibits coherent enhancements with the

oscillations in geomagnetic activity during both the day and night times. However, the electron density response between 200 and 350 km altitudes is dominated by the changes in the neutral composition and exhibits significant latitudinal, local time and seasonal variations. The results are discussed in light of equatorward wind perturbations during enhanced geomagnetic activity and summer-to-winter transequatorial neutral wind patterns.

1. Introduction

Understanding the complex interplay between the solar variability and space weather is very important for forecasting the disturbances in the Geospace environment that can affect the astronauts in space, payloads on board the satellites, space based communication and navigational systems as well as ground based power grid systems. The Coronal Mass Ejections (CMEs) and solar flares are the sources of high energy particles and are of primary importance because of their huge and immediate impact on the Earth. Further, the Coronal Holes (CHs) on the Sun, the principal sources of high speed solar wind particles, are another important source of geomagnetic disturbances on the Earth. The Coronal Holes are mainly unipolar magnetic field regions on the Sun with one foot print of field lines are attached to Sun and other are extending in to the interplanetary space giving rise to emission of high-speed solar wind streams [Krieger et al., 1973]. The proton density in CHs is typically 2 – 3 times lower than that of the quiet Sun and the temperature is around 10^5 - 10^6 K [Munro and Withbroe, 1972]. Due to their low density and emission measure, CHs can be identified as dark areas on X-ray and EUV images of the Sun and dominant unipolar regions on magnetograms [Reeves and Parkinson, 1970; Wiegelmann and Solanki, 2004]. When the interplanetary magnetic

field is oriented southward, strong coupling between the magnetized plasma within the high speed streams and Earth's magnetosphere results in transfer of mass, momentum and energy producing geomagnetic disturbances. Since the CHs rotate almost rigidly with the Sun, they produce recurrent high speed streams and geomagnetic disturbances in the Geospace environment [Timothy et al. 1975 and Tsurutani et al. 1995].

The coronal holes and solar wind streams undergo systematic variations over the 11-year solar cycle. Through much of the cycle, the Sun's polar region is dominated by coronal holes, the sources of large, persistent and fast solar wind streams with an average bulk speed of 500 – 800 km/s [Philips et al., 1995]. During the solar minimum, the polar holes became large and extend into equatorial and low latitude regions with some tongue-like extensions [Krieger et al., 1973; Sheeley and Harvey, 1981]. In addition to fast streams from polar holes, the solar wind has also dense low-speed streams (300 – 400 km/s) from the closed field regions near the equator, known as equatorial coronal streamer belt. As the streams travel in the interplanetary space, the high-speed streams catch the slow-speed streams and create regions of enhanced density and magnetic field, called co-rotating interaction regions (CIRs) [Tsurutani et al. 1995]. When the coronal high speed wind interacts with the preceding slow solar wind, forward and reverse shocks often form at the CIR boundaries. The CIR interfaces can be characterized by a relatively sharp density drop, temperature rise and a sharp increase in the solar wind bulk velocity. CIRs are especially prominent during the declining phase of the solar cycle, when the heliospheric magnetic field has a well-developed sector structure and coronal holes may extend to low latitudes [Richardson 2004].

The fast streams from the CHs and CIR interfaces have a tendency to repeat for several solar rotations producing recurrent geomagnetic activity at 27-day periodicity. However, recent investigations by Temmer et al. 2007 and Gibson et al. 2009 have elucidated that the solar wind velocity and geomagnetic properties also exhibit sub-harmonic solar rotational periodicities at 13.5-day, 9-day and even shorter periods during the descending and minimum phase of solar cycle 23. In response, the Earth's upper atmospheric properties such as thermospheric density and composition, plasma temperature, and electron density are also found to oscillate with the same periodicities [Lei et al., 2008a; Crowley et al., 2008; Sojka et al., 2009; Tulasi Ram et al., 2010].

The electron density in the ionosphere responds significantly to the changes in the thermosphere composition, neutral density, temperature, neutral winds as well as the electric fields, which in turn greatly varies with latitude, altitude, local time, season and the phase of the geomagnetic activity. Because of various neutral and electro-dynamic coupling processes are involved, the global ionospheric response to geomagnetic storms is much complex and been the subject of extensive investigations by both case studies as well as model simulations during the past 3-4 decades [Prolss, 1980; Fuller-Rowell et al., 1994, 1996; Buansanto 1999; Mendillo 2006 and the references therein]. However, the earlier studies on the altitudinal response of global ionosphere to geomagnetic storms were mostly based on the model simulations due to lack of global observations of vertical electron density profiles. Although the amplitude is smaller, the solar wind interfaces produce ionospheric changes similar to those associated with isolated geomagnetic storms [Mendillo and Schatter, 1983]. Hence, the short-period recurrent geomagnetic disturbances associated with periodic solar wind forcing during the low solar activity

periods provide an opportunity for a comprehensive investigation on the global scale ionospheric response to minor geomagnetic storms.

Therefore, the objective of the present investigation is for further understanding of periodic solar wind streams from recurrent coronal holes and its impact on Earth's geomagnetic and ionospheric properties. In this context, we first present the results of a systematic study of periodicities in the solar wind velocity and the area of coronal hole regions during the complete period of solar cycle 23. Secondly, we focus our investigation on extremely low solar activity period of 2008 to study the modulation of interplanetary solar wind parameters due to recurrent coronal holes and its imprints on the Earth's geomagnetic and ionospheric properties. Further, we present the seasonal dependence on the ionospheric response to recurrent geomagnetic activity associated with periodic solar wind forcing at different latitudinal-altitudinal regions.

2. Results and Discussion

2.1 Periodicities in the Solar wind velocity and the area of Coronal hole regions during the solar cycle 23

The solar wind (SW) velocity data from WIND and Atmospheric Composition Explorer (ACE) satellites during the period from the previous solar minimum to the minimum of SC23 (1996 to 2009), available through National Space Science Data Center's OMNIWeb interface (*http://nssdc.gsfc.nasa.gov/omniweb/*) has been considered in this study. The daily mean solar wind velocity data of 5114 consecutive days (14 – years) has been subjected to Morlet wavelet analysis to identify the various periodicities during different phases of the SC23. Figure 1(a) shows the daily variation of SW velocity (light blue line) and its 27-day running mean variation (thick blue line) from the

years 1996 to 2010. The daily variation of F10.7 solar flux (pink line) and its 27-day running mean variation are also shown in the same panel with right hand side scale to represent as a proxy to the solar activity variation during the SC23. It can be observed from this figure that the mean SW velocity during the previous solar minimum and the ascending phase of SC23 (1996 to late 2002) generally varies around 400 km/s (indicated by black dashed line). However, the mean SW velocity exhibits significantly larger values (420 to 600 km/s) during the descending phase of the SC23 (2003 to 2009) than ascending phase of SC23. This indicates that the source regions of high speed streams on the Sun are more populated and geo-effective during the descending phase of solar cycle than the ascending phase.

The Morlet wavelet power spectrum of daily mean SW velocity during the complete solar cycle (SC 23) is presented in the bottom panel [Fig. 1(b)]. It can be observed from this figure that the SW velocity exhibits periodicities at solar rotational (27-day) and its sub-harmonic periods (13.5-, 9- and 6.8-days) as indicated by horizontal pink dashed lines. The most interesting observation from the wavelet analysis is that the SW velocity has greater tendency to exhibit sub-harmonic solar rotational periodicities (13.5-, 9- and 6.8-days) during the same period where the SW velocity in general exhibits large values in Fig. 1(a), i.e., during the descending phase of SC23 (2003 to 2009). While these periodicities may also be observed during previous solar minimum and ascending phase of SC23, they occur occasionally and only for short periods. However during the descending phase, these sub-harmonic periodicities are observed for long and continuous patches with large spectral intensities.

138 The periodicities in the SW velocity can be explained by the longitudinal
139 distribution of CHs on the Sun in a straight forward manner. For example, Temmer et al.
140 [2007] and Lei et al. [2008b] have shown that the 9-day periodicity in the SW velocity in
141 2005 is mainly due to a triad of coronal holes at approximately 120^{o} apart in heliographic
142 longitude that persist for several rotations. Thus, with a view to further investigate the
143 spatial distribution of CHs on the Sun and the resultant periodicities in the SW properties
144 during different phase of SC23, the extreme ultraviolet images of the Sun have been
145 analyzed to compute the daily fractional CH area as described in Vrsnak et al. [2007] and
146 Temmer et al. [2007]. The daily images of the Sun at 195 Å from Extreme Ultraviolet
147 Imaging Telescope (EIT) on board the Solar and Heliospheric Observatory (SOHO)
148 during the period from June 1996 to 2006 and from Extreme Ultraviolet Imager (EUVI)
149 on board the Solar Terrestrial Relations Observatory (STEREO) during the period from
150 2007 to 2009 were considered in this study.
151 The coronal holes on the Sun are identified by threshold intensity detection
152 method described in Krista and Gallagher [2009]. In this method, the intensity
153 distribution (histogram) of the 195 Å image is constructed and the intensity
154 corresponding to the maximum in the histogram is considered as the quiet Sun intensity.
155 The threshold value for the detection of CHs is defined as the local minima in the
156 intensity histogram that are located within 30-70 % of the quiet Sun intensity and are
157 wider than 6 digital numbers (DNS). For those cases when the well defined minima
158 cannot be noticed, 40 % of the quiet Sun intensity is considered as the threshold to
159 identify the CHs. Since the thresholds are determined depending on the quiet Sun
160 intensity, this method is suitable during different phases of the solar cycle regardless of

161 the change in the overall intensity of Sun as well as independent of instrumental intensity
162 settings [Krista and Gallagher, 2009].

163 Figure 2 shows the typical examples of SOHO-EIT images at 195 Å during
164 ascending and descending phases of the SC 23 to illustrate the method of identification of
165 CHs on solar images for the computation of fractional CH area. The area covered by the
166 CHs in the central meridian slice between -10^o and 10^o heliographic longitudinal range
167 and between -60^o and 60^o heliographic latitudes (the area covered by pink contour line) is
168 computed for each day using the equation. (1).

169 $$\text{Fractional CH area} = \frac{\text{No. of pixels covered by CH in } [\pm 10^\circ \text{ h.long}, \pm 60^\circ \text{ h.lat}]}{\text{Total No. of pixels in } [\pm 10^\circ \text{ h.long}, \pm 60^\circ \text{ h.lat}]} \quad \text{----- (1)}$$

170 Here, the CH area between ± 60^o heliographic latitudes is only considered in order to
171 emphasize the effect of CHs which are extended equatorward as well as low-mid latitude
172 isolated CHs. In this analysis, one solar disk image at 195 Å for each day around 13 UT
173 is considered because of the satellite sampling time of SOHO and maximum availability
174 of data at 13 UT. For the days on which the image data was missing, we used an adjacent
175 longitudinal stripe from the previous/next day image whichever is available. Further
176 missing/bad data for less than 5 consecutive days are linearly interpolated to compute the
177 wavelet power spectrum (WPS). However, there are still some data gaps in the SOHO-
178 EIT data, hence, the WPS is computed only on continuous data segments of length more
179 than 50 days.

180 Figure 3(a) shows the daily variation of fractional CH area (light blue line) from
181 1996 to 2010 and its 27-day running mean variation (dark blue line). The corresponding
182 wavelet spectrum of CH area is presented in Fig. 3(b). The significant observation from
183 Fig. 3(a) is that the CH area computed between ± 60 heliographic latitudes also exhibits

large values from 2003 to 2009. The large values of SW velocity [Fig. 1(a)] and CH area [Fig. 3(a)] observed during the same period clearly indicates that the equatorward extension of polar holes and low latitude (probably isolated) coronal holes are more prominent during the descending phase of SC23 from 2003 to 2009. The fast solar wind streams from these coronal holes engulfed the Earth's environment resulting in large values of SW velocity as measured by ACE at L1 point. Further, the wavelet spectrum of CH area [Fig. 3(b)] also exhibits greater tendency to sub-harmonic periodicities at 13.5 and 9-days similar to that of SW velocity during the descending phase of SC23. These results indicate that a two to three large CH regions (either equatorward extended holes or isolated holes) that are longitudinally separated and persistent for several solar rotations have produced 13.5-day or 9-day periodicities in the CH area. The fast SW stream trajectories from these CHs engulf the geo-space environment and produce similar periodicities in SW velocity. Further, this feature is more prominent during the descending phase of the SC23. However, the exact one-to-one correlation of spectral intensities between CH area and SW may not be expected because the solar wind trajectories may some times perturbed by energetic events such as CMEs, solar flares and solar energetic particle events from the Sun. Even though the previous solar minimum (1996-1998) period has nearly the same solar activity (F10.7 solar flux) levels as the minimum of SC 23 (2005-2009), the values of both CH area and SW velocity are smaller during the previous solar minimum and the sub-harmonic periodicities are only occasionally observed for short periods.

2.2 Periodic modulation of interplanetary SW parameters and their imprints on Earth's geomagnetic activity during extreme solar minimum period, 2008.

We now focus our attention on the sub-harmonic periodicity of 9-day period as a diagnostic tool to study the periodic modulation in the interplanetary solar wind properties and their imprints on Earth's geomagnetic properties. The reasons for choosing the 9-day periodicity are explained in the next section. With a view to investigate the 9-day periodicity in the fractional CH area and its modulation on the interplanetary solar wind properties, the ACE's high resolution (64-second) Level-2 data during the solar minimum period in 2008 are carefully examined. This period was selected because the wavelet of both CH area and SW velocity exhibits strong 9-day periodicity during most of the year 2008 and also because of the availability of Formosat-3/COSMIC vertical electron density profile data to further study the seasonal dependence on latitudinal and altitudinal response of ionospheric electron density to this 9-day periodicity.

Figures 4(a) to (h) shows the fractional CH area derived from STEREO-EUVI images along with SW bulk velocity, SW magnetic field magnitude, |B|, SW proton temperature, SW proton density, vertical component, IMF Bz, symmetrical ring current index, SymH and geomagnetic activity index, Kp, respectively, during 2008. Although the 9-day periodicity in SW velocity can be seen almost throughout the year 2008, the data pertaining to the day numbers 1 to 120 are only shown in figure 4 for better visibility. It can be seen from this figure that the variation of SW velocity corresponds well with the variation of CH area with a phase delay of 2-3 days. This phase delay generally agrees with the travelling time of SW particles from the source to orbit of ACE

at L1-point. A careful examination of figures 4(b) to 4(e) reveals that the interplanetary SW properties exhibit the signatures of a series of co-rotating interaction regions (CIRs) during this period. It can be observed from these figures that, every sharp increase in SW velocity corresponds with a sharp increase in magnetic field magnitude, sharp increase in SW proton temperature and a sharp decrease in SW proton density, which are the signatures of CIR stream interface [Richardson et al. 1996, 1998, Tsurutani et al. 2006, 2008, Choi et al. 2009]. Further, the impulse type increase-and-decrease of magnetic field magnitude, proton density preceding-and-after the increase of SW velocity indicates the signatures of forward and reverse shocks associated with CIRs [Kennel et al. 1985, Tsurutani et al. 2006, 2008 and Choi et al. 2009]. Lei et al. [2010] have made a detailed investigation on the interplanetary solar wind parameters during 2008 and identified the presence of 38 CIRs in the entire year 2008 using the method described in McPherron et al. [2009]. Thus, the results from the figures 4(a)-(e) and the results from Lei et al. [2010] indicate that a series of CIRs are formed at quasi 9-day periodicity because of the interaction of fast solar wind stream trajectories from the equatorward extended or low-latitude (probably isolated) coronal holes with the preceding ambient slow solar wind streams. The resultant CIR structures of enhanced density and magnetic field regions impinge upon the Earth's magnetosphere and can trigger recurrent geomagnetic activity at quasi 9-day periodicity. For instance, from Figs. 4(g), it can be observed that a series of recurrent geomagnetic storms of weak to moderate intensities (SymH $\leq$ -30 to -50 nT) occurred throughout this period. A good correlation between the large positive and negative excursions of IMF Bz and the corresponding decrease in SymH index as well as simultaneous increase in Kp-index can be observed from figures 4(f), 4(g) and 4(h).

Because of highly oscillatory nature of Bz component with in CIRs [Fig. 4(f)], the resultant geomagnetic storms are typically only weak to moderate intensity. However, the recovery phases of these storms are elongated for several days or more as can be seen from Fig. 4(g).

The Lomb-Scargle (LS) amplitude spectra [Lomb, 1976; Scargle, 1982] of various parameters that described previously such as CH area, SW velocity, SW magnetic field magnitude (|B|), IMF Bz, SymH index, Kp-Index during the entire year of 2008 are presented in Figs. 5(a) to (f) respectively. Further, the LS spectra of Total Solar Irradiance (TSI) and EUV irradiance at 5-105 nm wavelengths are also shown for comparison in Figs. 5(g) and 5(h), respectively. Here, the TSI data is obtained from the measurements of TIM instrument on board the SORCE satellite and EUV irradiance data is obtained from the level-3 data products of Solar EUV Experiment (SEE) on board the TIMED satellite. It can be clearly observed from this figure that the CH area, solar wind parameters (SW velocity and SW magnetic field) as well as the geomagnetic activity indices (SymH and Kp indices) exhibit pronounced spectral peaks at 13.5 and 9-day periods. Further, the 9-day periodicity is strongly present in SW total magnetic field |B| due to compression effects at the beginning of the CIRs. However, the 9-day periodicity is absent in the vertical component Bz. This could be due to the large positive and negative fluctuations in IMF Bz [Fig. 4(f)] at stream-stream compression regions, which are the typical signatures of CIRs as described by Tsurutani 2005, 2006 and references therein. On the other hand, the Total Solar Irradiance (TSI) and EUV irradiance do not exhibit any significant spectral peaks at 13.5 and 9-day periods [Figs. 5(g) and 5(h)]. Thus, the results presented in Figs. 4 and 5 clearly indicate that these sub-harmonic solar

rotational periodicities at 13.5 and 9-day periods in geomagnetic activity indices (SymH and Kp) are primarily due to solar wind energy input associated with fast solar wind streams from the recurrent coronal holes. The solar wind high-speed streams (HSS) contain large-amplitude non-linear Alfven waves within the CIRs [Tsurutani et al. 1994, Balogh et al. 1995]. The negative Bz components of the Alfven waves within the high-speed streams lead to magnetic reconnection and transfer of energy from solar wind to the magnetosphere [Tsurutani and Gonzalez, 1987; Tsurutani et al. 2006], which is characterized by continuous auroral activity called as "High-Intensity Long Duration Continuous AE Activity (HILDCAA)". The magnetic reconnection associated with the Alfven waves cause continuous, shallow injections of solar wind plasma into the magnetosphere at auroral and mid latitudes. Further, the Kp-index which is a useful parameter to represent the particle precipitation at auroral and mid latitudes [Emery et al. 2008 and Emery et al. 2009] also exhibit coherent enhancements with SW velocity [Figs. 4(b) and 4(h)]. Therefore, the results from Figs. 4 and 5 clearly suggests that the fast solar wind trajectories from CHs, enhanced magnetic field associated with CIRs and Alfven wave associated magnetic field fluctuations in HSS-CIR structures trigger recurrent geomagnetic activity of weak to moderate levels in the geo-space environment.

During the ascending phase and solar maximum, the high speed streams narrow and weaken because of poleward shrinkage of coronal holes (for example, as can be seen from Fig. 2(a)). Additionally, the ambient solar wind flow is frequently perturbed by energetic events on the Sun such as coronal mass ejections (CME) and solar flares. Hence, the CME-associated geomagnetic storms can occur more frequently near the solar maximum. Whereas the occurrence rate of HSS-CIR associated recurrent geomagnetic

299 storms maximizes during the declining phase and solar minimum [Tsurutani et al. 2006]
300 due to the equatorward extended and/or low latitude isolated coronal holes as can be
301 observed in Fig. 2(b). During the solar minimum in 2008, the Sun was exceptionally
302 quiet with more than 70% of spotless days (annual average sunspot number was only 3)
303 and global weakness in the heliospheric magnetic field [Gibson et al. 2009]. However,
304 the large areas of low-mid latitude CHs and high speed streams [Figs. 4(a) and 4(b)] are
305 persistent for several solar rotations resulting in recurrent HSS-CIR associated
306 geomagnetic storms during 2008 [Fig. 4(g) and 4(h)]. It should be mentioned here that
307 albeit the solar wind and geomagnetic activity indices are shown for only day numbers 1
308 to 120 in 2008 in Fig. 4 for better visibility, the HSS-CIR associated geomagnetic storms
309 of moderate levels are observed almost throughout the year 2008 [for example, Lei et al.
310 2010].

311 **2.3. The global ionospheric response to recurrent geomagnetic activity at quasi 9-**
312 **day periods associated with HSS-CIR structures**

313 We now turn our investigation on the effects of this recurrent geomagnetic
314 activity on the ionospheric electron density using the global vertical electron density
315 observations of Formosat-3/COSMIC radio occultation measurements. The Formosat-
316 3/COSMIC, in short F3/C, is a constellation of six micro satellites orbiting around 800
317 km altitude, 72^{o} inclination angle, and 30^{o} separation in longitude. Each F3/C satellite
318 has a GPS Occultation eXperiment (GOX) payload, performing the radio occultation
319 observations in the ionosphere and provides ~ 2000 vertical electron density profiles per
320 day which are uniformly distributed all over the globe. The details of inversion and
321 validation of Ne(h) profiles can be found elsewhere [Schreiner et al. 1999 and 2007, Hajj

et al. 2000, Syndergaard et al. 2006 and Lei et al. 2007]. In the present study, the Ne(h) profiles during the entire year of 2008 were considered. All the vertical electron density profiles measured in each day are separated on solar local time (SLT) into day ($06 \leq$ SLT <18 hrs) and night ($18 \leq$ SLT < 06 hrs of next UT day) time observations. The separated density profiles are then zonally (longitudinally) averaged into 32 latitudinal bins from -80^o to +80^o geomagnetic latitudes (with 5^o window) and 30 altitudinal bins from 200 to 500 km (with 10 km window). The electron density profile data below 200 km were not considered in this study as the F3/C electron density data in the E- and F1-regions are often found to deviate from the ground based observations [Kelley, 2009, Liu et al. 2010]. Each binned time series of data are further spectral analyzed using the Lomb-Scargle (LS) algorithm to examine the periodicities in the zonal mean electron density.

For example, the zonal mean electron density at 300 km altitude during both day and night times are plotted as a function of geomagnetic latitude and day number in the year 2008, and presented in Figs. 6(a) and 6(b), respectively. The overlapped black curve in these figures is the variation of daily mean geomagnetic activity index, Kp in 2008. It can be seen from the Figs. 6(a) and 6(b), that the electron density exhibits large time scale seasonal and semi-annual variations as well as shorter time scale (multi-day) oscillations during both day and night times. Further, these shorter time scale oscillations in electron density corresponds well with the variations of daily mean geomagnetic activity index, Kp as may be seen from Figs. 6(a) and 6(b). In order to further examine the multi-day periodicities in the zonal mean electron density, Lomb-Scargle (LS) analysis is performed at each latitudinal bin and the periodograms are shown in Figs. 6(c) and 6(d) for day and night times, respectively. The LS periodogram of the daily mean geomagnetic activity

345 index, Kp is also overlapped (black curve with right hand scale) in Figs. 6(c) and 6(d) in
346 order to examine the relationship between the periodicities in the electron density and the
347 geomagnetic activity. Predominant spectral amplitudes are evident at solar rotational
348 (27-day) and its sub-harmonic periods (13.5-day and 9-days) during both day and night
349 times from -80^o to 80^o geomagnetic latitudes. Further, the spectral amplitudes at these
350 periodicities correspond extremely well with the periodicities in the geomagnetic activity
351 index (Kp). Note that the EUV irradiance from TIMED SEE does not exhibit any
352 significant spectral peaks at 13.5 and 9-day periods [Fig. 5(h)] during this period.

353 Thus, these results elucidate the periodic oscillations in both day and night side
354 ionospheric electron densities at solar rotational and its sub-harmonic periodicities in
355 support of earlier observations by Hocke [2008] and Lei et al. [2008c] in global mean
356 total electron content (TEC). Hocke [2008] showed a perfect correlation in the 27 and
357 13.5-day oscillations between global mean TEC and solar EUV and further suggested
358 that the other mechanisms rather than solar irradiation should contribute to the 9-, and 7-
359 day periodicities as these periodicities are absent in solar EUV spectrum. Later, Lei et al.
360 [2008c] have shown that the pronounced periodicities of 9- and 7-days in global mean
361 TEC are associated with solar wind high speed streams and geomagnetic activity. Hence,
362 the present results observed in the zonal mean electron density at 300 km corroborate
363 with the results observed by Lei et al. [2008c] in global mean TEC. Although the 27-day
364 and 13.5-day periodicities are present, they cannot be mainly attributed to recurrent
365 geomagnetic activity as 27-day and 13.5-day periodicities also exist in F10.7 solar flux
366 [Liang et al. 2008] which have a direct impact on the ion production. Therefore, we
367 focus on the important feature of 9-day periodicity in electron density and Kp as a

368 diagnostic tool to investigate the global ionospheric response to HSS-CIR associated
369 recurrent geomagnetic activity. There is also a significant peak observed at ~ 14-15 days
370 in the electron density periodograms during both day and night times [Figs. 6(c) and
371 6(d)]. It can be speculated that this 14-15 day periodicity in the electron density could be
372 possibly due to planetary wave oscillations in the lower thermosphere [Altadill and
373 Apostolov, 2003]. Since the focus of current investigation is on sub-harmonic solar
374 rotational periodicities, the spectral peak at ~14-15 day periodicity is not further
375 discussed.

376 With a view to examine the phase relationship between the 9-day periodicities in
377 the F-region ionosphere and the geomagnetic activity index (Kp) during different local
378 times and seasons, the electron density oscillations corresponding to 9-day periodicities at
379 each latitude-altitude bins are spectral filtered using a digital band pass filter centered at
380 9-days. Figure 7 shows the latitudinal variations of band pass filtered 9-day quasi-
381 periodic perturbations in the electron density at 300 km altitude during both day times
382 (left panels) and night times (right panels). The electron density perturbations
383 corresponding to 45-days at each season are separately shown in Figs. 7a-f. Figures 7(a)
384 and 7(b) correspond to day numbers 50-95 (equinox), Figures 7(c) and 7(d) correspond to
385 day numbers 155-200 (June solstice) and Figures 7(e) and 7(f) correspond to day
386 numbers 300-345 (December solstice). The day numbers in each season were carefully
387 selected as the wavelet spectra of both solar wind velocity (Fig.1) and Kp-index (not
388 shown in figure) exhibit strong spectral amplitudes at 9-day periodicity during those
389 days. The overlapped black curve in each panel is the bandpass filtered 9-day
390 perturbations in the Kp-index during the respective days. The perturbations in electron

density are expressed in relative percentage with respect to background levels (11-day running averaged electron density). From Fig. 7, it can be noticed that the amplitudes of electron density perturbations are slightly larger during the night than during the day. Also, the density perturbations are larger in the winter hemisphere than in the summer hemisphere and often exceed 40% of background levels. The larger percentage density perturbations could be due to smaller background electron densities during the night and at respective winter hemispheres as can be observed from Figs. 6(a) and 6(b).

Interestingly, the latitudinal variations in the band pass filtered electron density perturbations exhibit different phase relationship with the perturbations in Kp during different seasons. One consistent feature that can be observed during all the seasons is that the electron density perturbations are in-phase with the perturbations in Kp at low latitudes and out-of-phase at high latitudes during both day and night. This latitudinal variation is consistent with the changes in ΣO/N2 ratio observed by Crowley et al. [2008], N_mF2 variations observed by Tulasi Ram et al. [2010] and night time total electron content variations observed by Pedatella et al. [2010]. However, the latitudinal extent in which the electron density perturbations exhibit in-phase/out-of-phase relationship with Kp exhibits significant seasonal and local time dependence. During the equinox, the electron density perturbations are in-phase with Kp at low and mid-latitudes (0 to $\pm 40^o$ geomagnetic latitudes), which then smoothly varies with latitude and become out-of-phase with Kp at high latitudes ($\pm$ 60^o to $\pm 80^o$ geomagnetic latitudes) during day times [Fig. 7(a)]. During night times, the negative phase relationship at high latitudes appears to extend into low latitudes in the southern hemisphere [Fig. 7(b)]. During the June solstice, the density perturbations are clearly out-of-phase in the summer (northern)

414 hemisphere above +40^{o}N geomagnetic latitudes during the day [Fig. 7(c)] and almost
415 from geomagnetic equator during the night [Fig. 7(d)]. On the other hand, the density
416 perturbations in the winter (southern) hemisphere exhibit in-phase relationship with Kp
417 up to 60^{o}S geomagnetic latitudes during both day and night. During the December
418 solstice, the perturbations are in-phase between 40^{o}S and 40^{o}N geomagnetic latitudes and
419 are out-of-phase at high latitudes ($\pm$ 60^{o} to $\pm$80^{o} geomagnetic latitudes) during the day
420 [Fig. 7(e)]. Where as at night times, the negative phase zone penetrates deep in to low
421 latitudes in the summer (southern) hemisphere and the same is confined to higher
422 latitudes (65-80^{o}N) in the winter (northern) hemisphere [Fig. 7(f)].

423 Figure 8 is similar to that of Fig. 7 except at a different height of 450 km altitude.
424 It can be noticed that the latitudinal variation of electron density perturbations and their
425 phase relationship with Kp at 450 km is quite different from that at 300 km. At 450 km
426 altitude [Fig. 8], the electron density perturbations are in-phase with the perturbations in
427 Kp and the negative phase relationship is mostly confined to high latitudes of summer
428 hemisphere. During the equinoxes [Figs. 8(a) and 8(b)], the density perturbations exhibit
429 in-phase relationship with Kp almost at all latitudes. These results indicate that the
430 ionospheric electron density response to 9-day quasi periodic geomagnetic activity is not
431 globally symmetric unlike the thermospheric mass density response as shown by Lei et
432 al. [2008b] and Thayer et al. [2008]. Instead, the ionospheric response exhibits
433 significant variation with latitude, altitude, local time as well as with season.

434 It was known that the upwelling neutral winds during geomagnetic storms carries
435 molecular-rich air across the pressure level to higher altitudes leading to the reduction in
436 O/N_2 density ratio at high latitudes [Fuller-Rowell et al. 1994]. Also, the downwelling

437 wind transports atomic-oxygen-rich air parcels to low altitudes and enhances the O/N_2
438 density ratio at low latitudes [Strickland et al. 2001]. Thus, the out-of-phase (negative)
439 response at high latitudes and in-phase (positive) response at low latitudes observed at
440 300 km [Fig. 7] can be attributed as due to changes in the storm time composition
441 disturbances due to upwelling/downwelling at high/low latitudes [Crowley et al. 2008].
442 Further, the results from Figs. 7 and 8 indicates that the region of disturbed composition
443 zone (negative phase response) penetrates deep into lower latitudes at 300 km (around
444 F2-layer peak altitudes) and limits to higher latitudes at 450 km (topside ionosphere).
445 Also, the latitudinal extent of composition disturbance zone is found to vary with local
446 time as well as with season [Figs. 7 and 8].

447 In order to examine up to what latitudinal and altitudinal extent that the
448 composition changes may affect during different seasons and local times, we proceed
449 with the cross correlation analysis. The bandpass filtered 9-day periodic perturbations in
450 electron density at each latitude-altitude bin are cross correlated with the perturbations in
451 Kp and the zero-lag correlation coefficient is plotted as a function of latitude and altitude
452 during the respective seasons and local times as shown in Fig. 9. The positive correlation
453 coefficient indicate the enhancements in the electron density coherently with the
454 enhancements in the geomagnetic activity (positive response) and the negative correlation
455 indicate the reduction in electron density in response to enhanced geomagnetic activity
456 (negative response). It can be seen from this figure that the correlation coefficient in the
457 topside ionosphere (above 350 km) is positive except at high latitudes of northern
458 summer hemisphere. The positive response in the topside ionosphere can be attributed to
459 the thermal expansion of upper atmosphere and subsequent increase in the scale height

460 resulting from the enhanced plasma temperatures [Lei et al. 2008c, Sojka et al. 2009 and
461 Tulasi Ram et al. 2010]. Further, it can be noticed from Fig. 9 is that the latitudinal and
462 altitudinal extent of negative phase response due to disturbed neutral composition shows
463 significant seasonal and local time dependence. One prominent feature that can be
464 observed from Figs. 9(c)-(f) is that the region of negative correlation extends in to low
465 and equatorial latitudes in the summer hemisphere during both the day and night times.
466 Where as in the winter hemisphere, the negative correlation region is limited to high
467 latitudes (> ~60^{o}) during the day [Figs. 9(c) and 9(e)] and confined only to polar region
468 during the night times [Figs. 9(d) and 9(f)]. These results clearly suggests that the
469 disturbed composition changes due to upwelling winds at high latitudes penetrates deeper
470 into low and equatorial latitudes in the summer hemisphere than in the winter
471 hemisphere.

472 When the Joule and particle heating occur at high latitudes during the
473 geomagnetic activity associated with recurrent high speed solar wind forcing, the heated
474 thermosphere expands and leads to an increase in the neutral scale height (kT/mg).
475 While the larger effect is at high latitude, the atmospheric pressure tends to equilibrate
476 globally, the corresponding expansion occurs at all latitudes. Recently, Sojka et al [2009]
477 have shown that the ion temperature measured at 300 km shows strong enhancements
478 associated with CIRs in high speed solar wind streams. Plasma temperature changes
479 would cause similar changes in the plasma scale height, which is a measure of thickness
480 of the ionosphere. The increase in the scale height due to thermal expansion associated
481 with plasma temperature will cause similar increase in the F2-layer peak altitudes (h_mF2).
482 For example, Tulasi Ram et al. [2010] have also shown the 9-day quasi periodic

483 enhancements in the daytime topside ionospheric thickness (H_T) and the F2-layer peak
484 altitude (h_mF2) coherently with the geomagnetic activity (Kp) at all latitudes. Therefore,
485 when one measures the electron density at any fixed height in the topside ionosphere, the
486 increase/decrease in the scale height and h_mF2 causes corresponding increase/decrease of
487 electron density. Thus, the observed positive response in the topside ionosphere (above
488 350 km altitude) in Fig. 9 is related to corresponding changes in the scale height and
489 h_mF2 due to thermal expansion associated with plasma temperature. Further, the
490 equatorward wind during enhanced geomagnetic activity will also raise the F-layer to
491 higher altitudes. This would also contribute to the coherent enhancements in the h_mF2 as
492 observed by Tulasi Ram et al. [2010]. However, the upwelling wind during enhanced
493 geomagnetic activity carries the molecular rich air to higher altitudes at the same time
494 leading to a decrease in O/N_2 ratio. The electron density near F2-layer peak altitudes is
495 mostly determined by the balance of production due to photoionization of O and loss due
496 to N_2 [Rishbeth and Garriott, 1969]. Thus, the electron density at F2 peak altitudes
497 responds to changes in neutral composition (O/N_2 density ratio) brought about by the
498 upwelling/downwelling winds at high/low latitudes during the enhanced geomagnetic
499 activity. The dominant process driving the electron density changes in the night time
500 ionosphere is the loss through recombination. Thus, the changes in N_2 and O_2
501 concentrations due to upwelling will modify the chemical loss rates and in turn electron
502 densities. Therefore, the electron density response around 200 to 350 km is dominated by
503 the changes in neutral composition brought about by the global thermospheric circulation.
504 Further, there will be a mean transequatorial neutral wind from the summer
505 hemisphere to winter hemisphere during the solstices. Also, the summer-to-winter

transequatorial neutral wind maximizes during the night due to reduced ion-drag. The summer-to-winter hemispheric wind will be in same direction to the equatorward wind in the summer hemisphere. On the other hand, the summer-to-winter hemispheric wind is in the opposite direction to the equatorward wind in the winter hemisphere. Thus, the latitudinal and altitudinal extent of disturbed composition changes observed in Fig. 9 depends on the relative strengths and directions of the summer-to-winter transequatorial wind and the equatorward wind due to high latitude heating during the periods of enhanced geomagnetic activity [Buansanto 1999]. In the summer hemisphere, the total wind is augmented by the prevailing summer-to-winter transequatorial wind and thus causes the composition disturbance zone to extend deep into low and equatorial latitudes as may be seen from Figs. 9(c)-(f). However, the summer-to-winter wind impedes the equatorward motion of the composition changes in the winter hemisphere. Thus, the negative phase response in the winter hemisphere is limited to high latitudes (~ 60^{o}) during the day time [Figs. 9(c) and 9(e)]. Further, the disturbed composition zone is limited only to polar region during the night time [Figs. 9(d) and 9(f)]. This could be possibly due to large oppositely acting transequatorial summer-to-winter winds during the night times.

3. Summary

A comprehensive investigation on the solar rotational and its sub-harmonic periodicities in coronal hole regions and solar wind velocity has been carried out, for the first time, using the solar EUV image data from the complete solar cycle 23 and its impact on the Earth's geomagnetic and ionospheric electron density have been studied

528 during the extreme solar minimum period, 2008. The important observations and results
529 are herein summarized in the following paragraphs.

530 Both the solar wind velocity [Fig. 1(a)] and fractional CH area [Fig. 3(a)]
531 consistently exhibit similar features with large values during the declining phase and the
532 minimum of SC 23 indicating that the equatorward extension of polar holes and low-
533 latitude (probably isolated) holes are prevailing during the declining phase of SC 23 (i.e.,
534 from 2003-2009). Further, both the SW velocity as well as the CH area exhibit greater
535 tendency for sub-harmonic (13.5-day and 9-day) periodicities during the declining phase
536 and minimum of SC 23. This suggests two/three large CH regions that longitudinally
537 distributed by $180^{o}/120^{o}$ apart and persistent for several rotations may produce sub-
538 harmonic periodicities in the fractional CH area. This feature is more prominent during
539 the declining phase and solar minimum because of the equatorward extension of polar
540 holes or low-latitude isolated holes. Even though the previous solar minimum (1996-
541 1998) period has the nearly the same solar activity (F10.7 solar flux) levels as the
542 minimum of SC 23 (2005-2009), the values of both CH area and SW velocity are smaller
543 during the previous solar minimum and the sub-harmonic periodicities are only
544 occasionally observed for short periods [Figs. 1 and 3]. This speculates that the
545 frequently observed, long lasting (several solar rotations) sub-harmonic periodicities in
546 CH area and SW properties during the declining phase from 2003 to 2009 [Figs. 1(b) and
547 3(b)] may probably be a unique feature of SC 23. The recurrent solar wind high speed
548 streams (HSS) from the several rotations of equatorward extended or low-latitude
549 (probably isolated) coronal holes interact with the preceding ambient slow solar wind
550 stream and produce recurrent co-rotating interaction regions (CIRs). The resultant HSS-

551 CIR structures of enhanced density and magnetic field regions recurrently impinge upon
552 the Earth's magnetosphere. The magnetic reconnection associated with the Alfven waves
553 in the HSS-CIR structures cause continuous, shallow injections of solar wind plasma into
554 the magnetosphere and trigger recurrent geomagnetic activity of weak to moderate levels
555 in the geo-space environment [Fig. 4]. Further, the LS amplitude spectra [Fig. 5] of CH
556 area, SW parameters and geomagnetic activity indices (SymH and Kp) show similar
557 features with strong spectral peaks at 13.5 and 9-day periods. The results from Figs. 4
558 and 5 clearly suggests that the sub-harmonic solar rotational periodicities in the
559 geomagnetic activity (SymH and Kp indices) are primarily due to solar wind energy input
560 associated with CIR structures within the fast solar wind streams from the recurrent
561 coronal holes.

562 The ionospheric electron density response to this HSS-CIR induced recurrent
563 geomagnetic activity has been investigated using the Formosat-3/COSMIC radio
564 occultation measurements during the extremely low solar activity year 2008. From Fig.7,
565 it was elucidated that the both day and night side electron densities exhibit periodic
566 oscillations at solar rotational (27-day) and its sub-harmonic periodicities (13.5 and 9-
567 day) in the electron density. Further, the spectral amplitudes of these oscillations in
568 ionospheric electron density correlate well with the oscillations in the geomagnetic
569 activity index, Kp. The important feature of 9-day periodicity in electron density and Kp
570 is considered as a diagnostic tool to investigate the global ionospheric response to HSS-
571 CIR associated recurrent geomagnetic activity. In general, the topside ionospheric
572 response (above 350 km) appears to be dominated by the changes in the plasma
573 temperature and/or scale height and exhibits coherent enhancements with the

perturbations in the Kp during both the day and night times. However, the electron density response between 200 and 350 km altitudes is dominated by the changes in the neutral composition and exhibits significant latitudinal, local time and seasonal variations. The upwelling winds at high latitudes significantly alters the neutral composition (O/N_2 density ratio) and results in a decrease in electron density during the enhanced geomagnetic activity. In the summer hemisphere, the composition disturbance zone penetrates deep into low and equatorial latitudes during both day and night times where the total wind is augmented by the summer-to-winter transequatorial wind. In the winter hemisphere, the summer-to-winter wind is in the opposite direction and limits the composition disturbance zone to high latitudes ($> \sim 60^o$) during the day time. Further, the enhanced transequatorial summer-to-winter wind during the night time restricts the composition disturbance zone only to polar region of winter hemisphere.

The recurrent geomagnetic disturbances associated with co-rotating interaction regions (CIR) in the solar wind high speed streams during the extreme solar minimum period, 2008 facilitates an opportunity to investigate the diurnal and seasonal dependence of the ionospheric response at different latitude and altitude regions. The results obtained from this investigation can be applicable to the global ionospheric response to minor (isolated) geomagnetic storms and thus provide some important insights to future modeling works on the ionosphere-thermosphere response to geomagnetic storms and solar wind-magnetosphere-ionosphere-thermosphere coupling processes.

4. Acknowledgements

S. Tulasi Ram is supported by post-doctoral fellowship from ASIAA, Academia Sinica. The authors acknowledge Prof. Xuepu Zhao and Prof. S. T. Wu for their useful

discussion and Dr. Jiuhou Lei for providing great help in the wavelet analysis. Further, we thank the two reviewers for their constructive comments and suggestions which greatly helped in improving the paper. The authors wish to thank UCAR/CDAAC, NSPO for providing FORMOSAT-3/COSMIC data. The authors also acknowledge the open data policy of SOHO-EIT, STEREO-EUV teams for solar image data, ACE Science Center and NSSDC for SW data, WDC for geomagnetic data, SORCE team for TSI data and TIMED-SEE team for EUV irradiance data.

5. References

Altadill, D., and E. M. Apostolov (2003), Time and scale size of planetary wave signatures in the ionospheric F region: Role of the geomagnetic activity and mesosphere/lower thermosphere winds, J. Geophys. Res., 108(A11), 1403-1415, doi:10.1029/2003JA010015.

Balogh, A., E. J. Smith, B. T. Tsurutani, D. J. Southwood, R. J. Forsyth, and T. S. Horbury (1995), The heliospheric magnetic field over the south polar region of the sun, *Science*, 268 (5218), 1007-1010.

Buonsanto, M. J., (1999), Ionospheric Storms - A Review, Space Sci. Rev., 88, 563-601.

Choi, Y., Y.-J. Moon, Seonghwan Choi, Ji-Hye Baek, Sungsoo S. Kim, K.-S. Cho, and G.S. Choe (2009), Statistical Analysis of the Relationships among Coronal Holes, Corotating Interaction Regions, and Geomagnetic Storms, *Sol. Phys.*, 254, 311–323, doi:10.1007/s11207-008-9296-3.

Crowley, G., A. Reynolds, J. P. Thayer, J. Lei, L. J. Paxton, A. B. Christensen, Y. Zhang, R. R. Meier, and D. J. Strickland (2008), Periodic modulations in thermospheric composition by solar wind high speed streams, *Geophys. Res. Lett*., 35, L21106,

doi:10.1029/2008GL035745.

Emery, B. A., V. Coumans, D. S. Evans, G. A. Germany, M. S. Greer, E. Holeman, K. Kadinsky-Cade, F. J. Rich, and W. Xu (2008), Seasonal, Kp, solar wind, and solar flux variations in long-term single-pass satellite estimates of electron and ion auroral hemispheric power, J. Geophys. Res., 113, A06311, doi:10.1029/2007JA012866.

Emery, B. A., I. G. Richardson, D. S. Evans, and F. J. Rich (2009), Solar wind structure sources and periodicities of auroral electron power over three solar cycles, J. Atmos. Sol. Terr. Phys., 71, 1157-1175.

Fuller-Rowell, T. J., M. V. Coderscu, H. Rishbeth, R. J. Moffett, and S. Quegan (1996), On the seasonal response of the thermosphere and ionosphere to geomagnetic storms, *J. Geophys. Res.*, 101, 2343-2353.

Fuller-Rowell, T. J., M. V. Codrescu, R. J. Moffett, and S. Quegan (1994), Response of the thermosphere and ionosphere to geomagnetic storms, *J. Geophys. Res.*, 99, 3893–3914.

Gibson, S. E., J. U. Kozyra, G. de Toma, B. A. Emery, T. Onsager, and B. J. Thompson (2009), If the Sun is so quiet, why is the Earth ringing? A comparison of two solar minimum intervals, *J. Geophys. Res.*, 114, A09105, doi:10.1029/2009JA014342.

Hajj. G. A, L. C. Lee, Xiaoqing Pi, L. J. Romans, W. S. Schreiner, P. R. Straus, Chunming Wang (2000), COSMIC GPS Ionospheric Sensing and Space Weather, *Terr. Atmos. and Oceanic. Sci.*, 11(1), 235-272.

Hocke, K. (2008), Oscillations of global mean TEC, *J. Geophys. Res.*, 113, A04302, doi:10.1029/2007JA012798.

Kelley, M. C., V. K. Wong, N. Aponte, C. Coker, A. J. Mannucci, and A. Komjathy (2009), Comparison of COSMIC occultation-based electron density profiles and TIP observations with Arecibo incoherent scatter radar data, *Radio Sci.*, 44, RS4011, doi:10.1029/2008RS004087.

Kennel, C. F., J. Arons, R. Blandford, F. Coroniti, M. Israel, L. Lanzerotti, A. Lightman, K. Papadopoulos, R. Rosner, and F. Scarf (1985), Perspectives on Space and Astrophysical Plasma Physics, Unstable Current Systems and Plasma Instabilities in Astrophysics, *IAU Symp.* (eds. M.R. Kundu and G.D. Holman), 537-552.

Krieger, A. S., A. F. Timothy, and E. C. Roelof (1973), A coronal hole and its identification as the source of a high velocity solar wind stream, *Sol. Phys.*, 29, 505–525.

Krista, L. D., and P. T. Gallagher (2009), Automated coronal hole detection using the local intensity thresholding techniques, *Sol. Phys.*, 256, 87-100, doi:10.1007/s11207-009-9357-2

Lei, J., et al. (2007), Comparison of COSMIC ionospheric measurements with ground-based observations and model predictions: Preliminary results, *J. Geophys. Res.*, 112, A07308, doi:10.1029/2006JA012240.

Lei, J., J. P. Thayer, J. M. Forbes, E. K. Sutton, and R. S. Nerem (2008a), Rotating solar coronal holes and periodic modulation of the upper atmosphere, *Geophys. Res. Lett.*, 35, L10109, doi:10.1029/2008GL033875.

Lei, J., J. P. Thayer, J. M. Forbes, E. K. Sutton, R. S. Nerem, M. Temmer, and A. Veronig (2008b), Global thermospheric density variations cause by high-speed solar

wind streams during the declining phase of solar cycle 23, *J. Geophys. Res.*,113, A11303, doi:10.1029/2008JA013433.

Lei, J., J. P. Thayer, J. M. Forbes, Q. Wu, C. She, W. Wan and W. Wang (2008c), Ionosphere response to solar wind high-speed streams, *Geophys. Res. Lett.,* 35, L19105, doi:10.1029/2008GL035208.

Lei, J., J. P. Thayer, W. Wang, R. L. McPherron (2010), Impact of CIR storms on Thermosphere density variability during the solar minimum of 2008, Sol. Phys., doi:10.1007/s11207-010-9563-y, in press.

Liang, M.-C., K.-F. Li, R.-L. Shia, and Y. L. Yung (2008), Short-period solar cycle signals in the ionosphere observed by FORMOSAT-3/COSMIC, *Geophys. Res. Lett.*, 35, L15818, doi:10.1029/2008GL034433.

Liu, J. Y., C. Y. Lin, C. H. Lin, H. F. Tsai, S. C. Solomon, Y. Y. Sun, I. T. Lee, W. S. Schreiner, and Y. H. Kuo (2010), Artificial Plasma Cave in the Low-latitude Ionosphere Results from the Radio Occultation Inversion of the FORMOSAT-3/COSMIC, J. *Geophys. Res*., doi:10.1029/2009JA015079 (in press).

Lomb, N. R. (1976), Least-squares frequency analysis of unequally spaced data, *Astrophys. Space Sci*., 39, 447– 462.

McPherron, R.L., D. N. Baker, N. U. Crooker (2009), Role of the Russell – McPherron effect in the acceleration of relativistic electrons. *J. Atmos. Solar-Terr. Phys.* 71, 1032-1044.

Mendillo, M. (2006), Storms in the ionosphere: Patterns and processes for total electron content, *Rev. Geophys*., 44, RG4001, doi:10.1029/2005RG000193.

Mendillo, M., and K. Schatten (1983), Influence of salar sector boundaries on

ionospheric variability, *J. Geophys. Res*., 88(A11), 9145-9153.

Munro, R.H. and G. L. Withbroe (1972), Properties of a coronal “hole” derived from extreme-ultraviolet observations, *Astrophys. J.* 176, 511-520.

Mursula, K., and B. Zieger (1996), The 13.5-day periodicity in the Sun, solar wind, and geomagnetic activity: The last three solar cycles, J. Geophys. Res., 101(A12), 27077-27090.

Pedatella, N. M., J. Lei, J. P. Thayer, and J. M. Forbes (2010), Ionosphere response to recurrent geomagnetic activity: Local time dependency, J. Geophys. Res., 115, A02301, doi:10.1029/2009JA014712.

Phillips J. L., S. J. Bame, W. C. Feldman et al. (1995), Ulysses Solar Wind plamsa observations at high southerly latitudes, Science 268 (5213), 1030-1033 (1995).

Prolss, G. W. (1980), Magnetic storm associated perturbation of the upper atmosphere: Recent results obtained by satellite-borne gas analyzers, *Rev. Geophys*., 18, 183–202.

Reeves, E.M., W. H. Parkinson (1970), An atlas of extreme-ultraviolet spectroheliograms from OSO-IV, *Astrophys. J. Suppl.* 21.1, 181.

Richardson, I. G. (2004), Energetic particles and corotating interaction region in the solar wind, *Space Sci. Rev.* 111, 267–376.

Richardson, I.G., G. Wibberenz, H. V. Cane (1996), The Relationship Between Recurring Cosmic Ray Depressions and Corotating SolarWind Streams at ≤ 1 AU: IMP 8 and Helios 1 and 2 Anti-Coincidence Guard Rate Observations, *J. Geophys. Res.* 101, 13483-13496.

Richardson, I.G., J. E. Mazur, G. M. Mason (1998), A comparison of recurrent energetic

ion enhancements observed at Ulysses and at 1AU by IMP-8 and SAMPEX: Ulysses launch until following the first north polar passage, *J. Geophys. Res.* 103, 2115-2130.

Rishbeth, H., and O. K. Garriott (1969), Introduction to Ionospheric Physics, pp. 1 – 331, Academic, New York.

Scargle, J. D. (1982), Studies in astronomical time series analysis. II. Statistical aspects of spectral analysis of unevenly spaced data, *Astrophys. J.*, 263, 835– 853.

Schreiner, W. S., S. V. Sokolovskiy, and C. Rocken (1999), Analysis and validation of GPS/MET radio occultation data in the ionosphere, *Radio Sci.*, 34, 949– 966.

Schreiner, W., C. Rocken, S. Sokolovskiy, S. Syndergaard, and D. Hunt (2007), Estimates of the precision of GPS radio occultations from the COSMIC/FORMOSAT-3 mission, *Geophys. Res. Lett.*, 34, L04808, doi:10.1029/2006GL027557.

Sheeley, N. R., Jr., and J. W. Harvey (1981), Coronal holes, solar wind streams, and recurrent geomagnetic disturbances during 1978 and 1979, *Sol. Phys.*, 70, 237–249.

Sojka, J. J., R. L. McPherron, A. P.van Eyken, M. J. Nicolls, C. J. Heinselman, and J. D. Kelly (2009), Observations of ionospheric heating during the passage of solar coronal hole fast streams, *Geophys. Res. Lett.*, 36, L19105, doi:10.1029/2009GL039064.

Strickland, D. J., R. E. Daniell, and J. D. Craven (2001), Negative ionospheric storm coincident with DE 1-observed thermospheric disturbance on October 14, 1981, *J. Geophys. Res.*, 106, 21,049– 21,062.

Syndergaard, S.,W. S. Schreiner, C. Rocken, D. C. Hunt, and K. F. Dymond (2006), Preparing for COSMIC: Inversion and analysis of ionospheric data products, in

Atmosphere and Climate: Studies by Occultation Methods, edited by U. Foelsche, G. Kirchengast, and A. K. Steiner, *Springer*, Berlin,137–146.

Temmer, M., B. Vrsnak, and A. M. Veronig (2007), Periodic appearance of coronal holes and the related variation of solar wind parameters, *Sol. Phys.*, 241, 371– 383, doi:10.1007/s11207-007-0336-1.

Thayer, J. P., J. Lei, J. M. Forbes, E. K. Sutton, and R. S. Nerem (2008), Thermospheric density oscillations due to periodic solar wind high-speed streams, *J. Geophys. Res.*, 113, A06307, doi:10.1029/2008JA013190.

Timothy, A.F., A. S. Krieger, G. S., Vaiana (1975), The structure and evolution of coronal holes, *Solar Phys.* 42, 135-156.

Tsurutani, B. T., and W. D. Gonzalez (1987), The cause of high intensity long-duration continuous AE activity (HILDCAAs): Interplanetary Alfven wave trains, *Planet. Space Sci.*, 35, 405

Tsurutani, B. T., C. M. Ho, E. J. Smith, M. Neugebauer, B. E. Goldstein, J. S. Mok, J. K. Arballo, A. Balogh, D. J. Southwood, and W. C. Feldman (1994), The relationship between interplanetary discontinuities and Alfven waves: Ulysses observations, *Geophys. Res. Lett.*, 21, 2267.

Tsurutani, B. T., E. Echer, F. L. Guarnieri, and J. U. Kozyra (2008), CAWSES November 7–8, 2004, superstorm: Complex solar and interplanetary features in the post- solar maximum phase, *Geophys. Res. Lett.*, *35*, L06S05, doi:10.1029/2007GL031473.

Tsurutani, B. T., et al. (2006), Corotating solar wind streams and recurrent geomagnetic activity: A review, *J. Geophys. Res.*, 111, A07S01, doi:10.1029/2005JA011273.

Tsurutani, B. T., W. D. Gonzalez, A. L. C. Gonzalez, F. Tang, J. K. Arballo, and M. Okada (1995), Interplanetary origin of geomagnetic activity in the declining phase of the solar cycle, *J. Geophys. Res.*, 100(A11), 21,717– 21,733.

Tulasi Ram, S., J. Lei, S.-Y. Su, C.H. Liu, C. H. Lin and W. S. Chen (2010), Dayside ionospheric response to recurrent geomagnetic activity during the extreme solar minimum of 2008, *Geophys. Res. Lett.*, 37, L02101, doi:10.1029/2009GL041038.

Vrsˇnak, B., M. Temmer, and A. M. Veronig (2007), Coronal holes and solar wind high-speed streams: I. Forecasting the solar wind parameters, *Sol. Phys.*, 240, 315– 330.

Wiegelmann, T., and S.K. Solanki (2004), Why are Coronal Holes Indistinguishable from the Quiet Sun in Transition Region Radiation? *Proc. SOHO 15 Workshop - Coronal Heating*, ESA SP-575, 35.

605

606

607

608

609

610

611

612

613

614

615 # Figure Captions

616 Fig. 1: (a) The daily mean variation of SW velocity (light blue) and F10.7 solar flux
617 (pink) along with their 27-day running mean variations during the years from
618 1996 to 2010. (b) The Morlet wavelet spectrum of SW velocity. The horizontal
619 pink dotted lines in Fig. 1(b) represent the periodicities corresponding to 27,
620 13.5, 9 and 6.8 days. The thin contour line in black color highlights the
621 spectrum above the 95% significance level. The vertical white dotted lines in
622 Fig. 1(b) indicate the cone of influence of the wavelet power spectrum. The
623 spectral intensities vary from dark blue (lowest) to dark red (highest).

624 Fig. 2: Typical examples of SOHO-EIT images at 195 Å during the ascending phase
625 (August 03, 2000) and descending phase (January 27, 2005) of the SC 23. Large
626 and isolated coronal holes can be seen at low latitudes during the descending
627 phase. CH regions on the Sun are identified by intensity thresholding and the
628 fractional CH area within the central meridian slice of $\pm 10^{o}$ heliographic
629 longitudes and $\pm 60^{o}$ heliographic latitudes (the area covered by pink contour line)
630 is considered on each day.

631 Fig. 3: (a) The daily variation of fractional CH area (light blue) along with their 27-day
632 running mean variations during the years from 1996 to 2010. (b) The Morlet
633 wavelet spectrum of CH area. The horizontal pink dotted lines in Fig. 3(b)
634 represent the periodicities corresponding to 27, 13.5, 9 and 6.8 days. The thin
635 contour line in black color highlights the spectrum above the 95% significance
636 level. The vertical white dotted lines in Fig. 1(b) indicate the cone of influence of

637 the wavelet power spectrum. The spectral intensities vary from dark blue (lowest)
638 to dark red (highest).

639 Fig. 4: The quasi 9-day periodic variation of (a) Fractional CH area, (b) SW bulk
640 velocity, (c) SW magnetic field magnitude, (d) SW proton temperature (e) SW
641 proton density, (f) vertical component IMF Bz, (g) ring current index, SymH and
642 (g) geomagnetic activity index, Kp during the extreme solar minimum period
643 from day number 1 to 120 in 2008.

644 Fig. 5: The Lomb-Scargle (LS) amplitude spectra of (a) Coronal Hole area, (b) Solar
645 Wind velocity, (c) Solar Wind magnetic field magnitude |B|, (d) vertical
646 component IMF Bz, (e) Kp-Index, (f) Sym-H index, (g) Total Solar Irradiance,
647 and (h) EUV irradiance at 50 – 105 nm during the extreme solar minimum year of
648 2008.

649 Fig. 6: The zonal mean electron density at 300 km altitude as a function of geomagnetic
650 latitude and day number in 2008 during day [Fig. 6(a)] and night times [Fig. 6(b)].
651 The unit for electron density is Ele/cm^3 in log scale. The corresponding Lomb-
652 Scargle (LS) periodograms are shown in Figs. 6(c) and 6(d). Daily mean Kp-
653 index and its LS spectral amplitudes are overlapped as black curves in the
654 respective panels (right hand scale).

655 Fig. 7: Bandpass filtered 9-day quasi periodic perturbations in zonal mean electron
656 density at 300 km altitude during equinoxes [Figs. 7(a) and 7(b)], northern
657 summer [Figs. 7(c) and 7(d)] and northern winter solstices [Figs. 7(e) and 7(f)].
658 The left hand panels correspond to day time and right hand panels correspond to
659 night time. The 9-day perturbations in Kp are also overlapped in each panel as

660 black curve with right hand scale. The electron density perturbations are
661 expressed in percentage with respect to 11-day running mean.
662 Fig. 8: Same as that of Fig. 7 except for 450 km altitude.
663 Fig. 9: (a) Latitudinal and altitudinal variation of correlation coefficient obtained from
664 the cross correlation of bandpass filtered 9-day perturbations in electron density
665 with the perturbations in Kp during equinoxes [Figs. 9(a) and 9(b)], northern
666 summer [Figs. 9(c) and 9(d)] and northern winter solstices [Figs. 9(e) and 9(f)].
667 The left hand panels correspond to day time and right hand panels correspond to
668 night time.

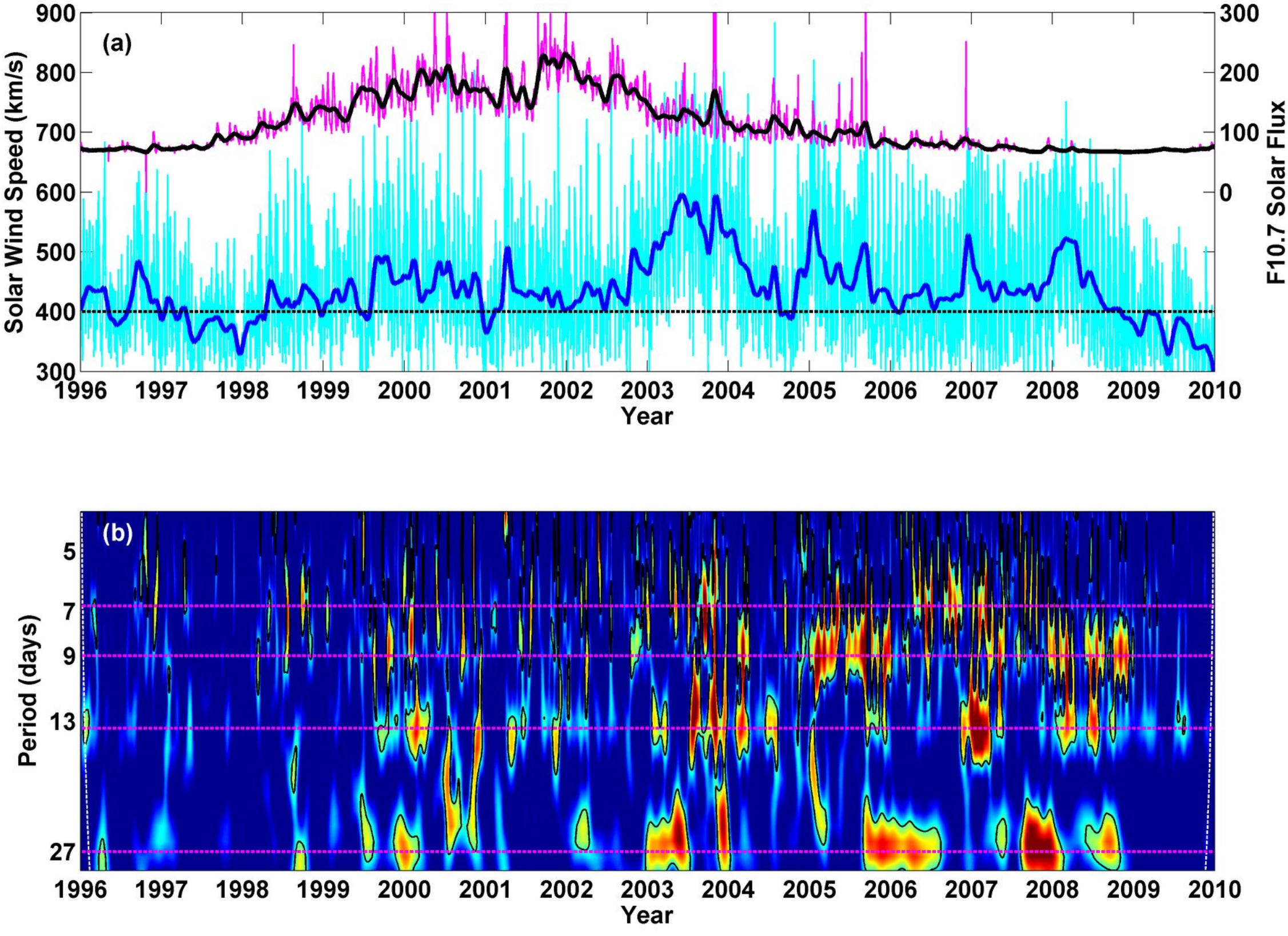
(a)
Solar Wind Speed (km/s)
F10.7 Solar Flux
900
800
700
600
500
400
300
300
200
100
0
1996
1997
1998
1999
2000
2001
2002
2003
2004
2005
2006
2007
2008
2009
2010
Year
(b)
Period (days)
5
7
9
13
27
1996
1997
1998
1999
2000
2001
2002
2003
2004
2005
2006
2007
2008
2009
2010
Year

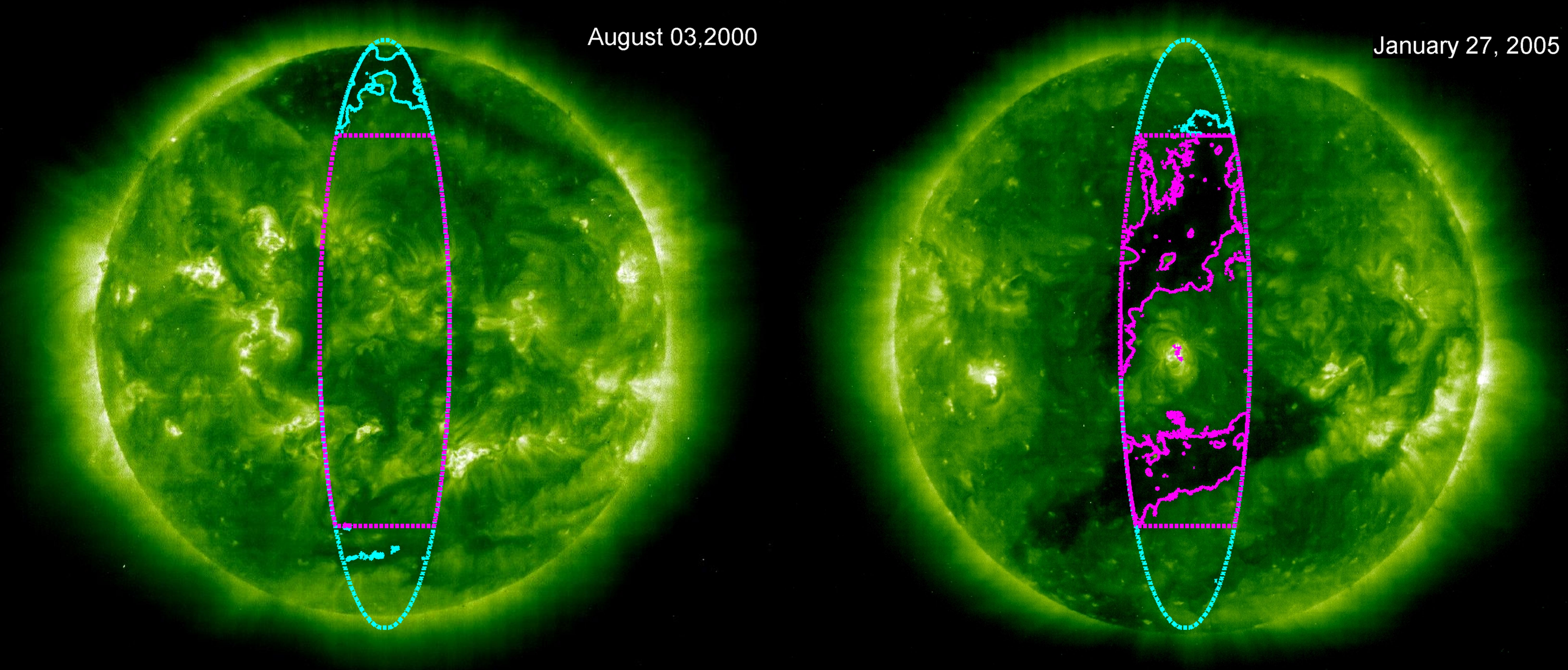
August 03,2000
January 27, 2005

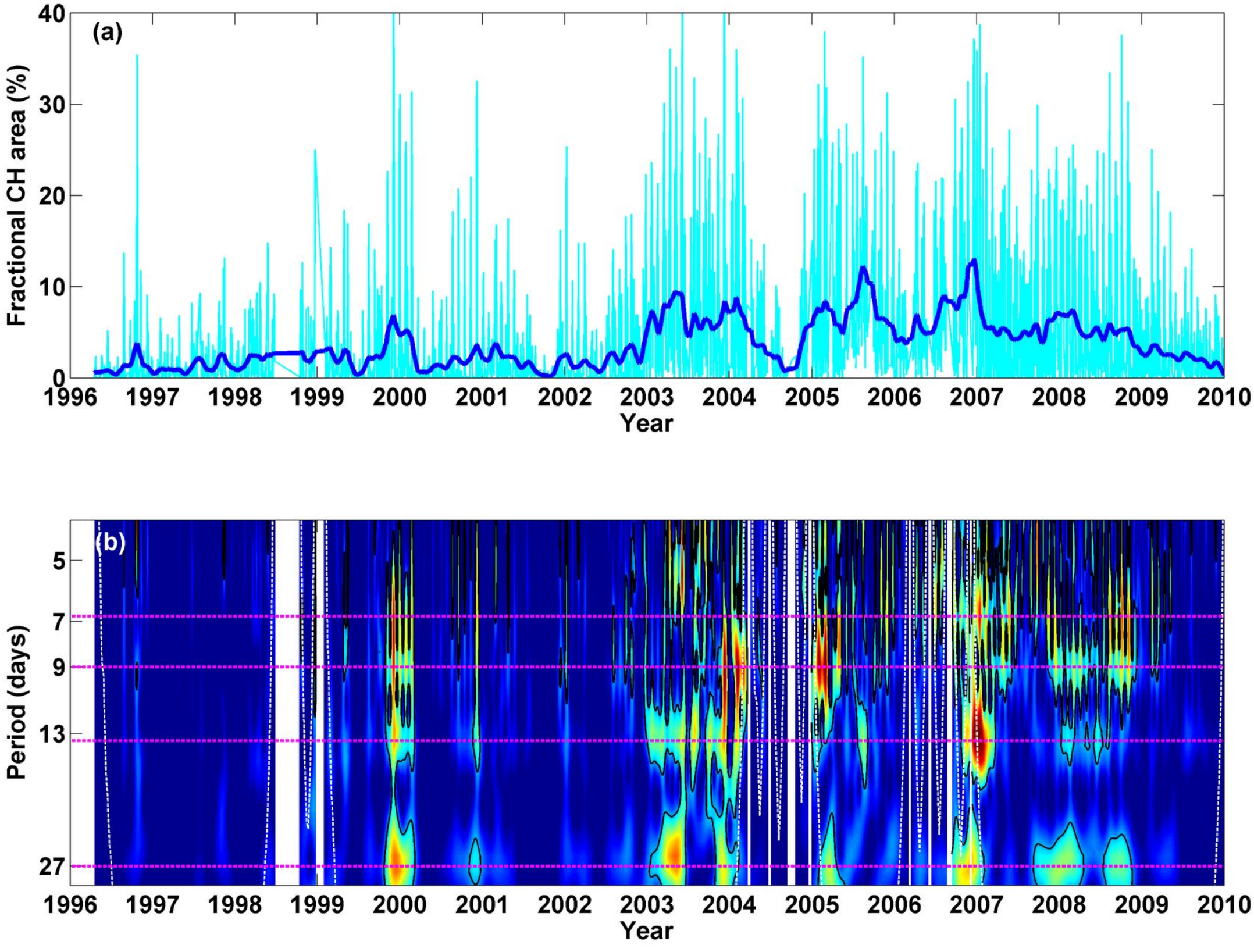
(a)
Fractional CH area (%)
0
10
20
30
40
1996
1997
1998
1999
2000
2001
2002
2003
2004
2005
2006
2007
2008
2009
2010
Year
(b)
Period (days)
5
7
9
13
27
1996
1997
1998
1999
2000
2001
2002
2003
2004
2005
2006
2007
2008
2009
2010
Year

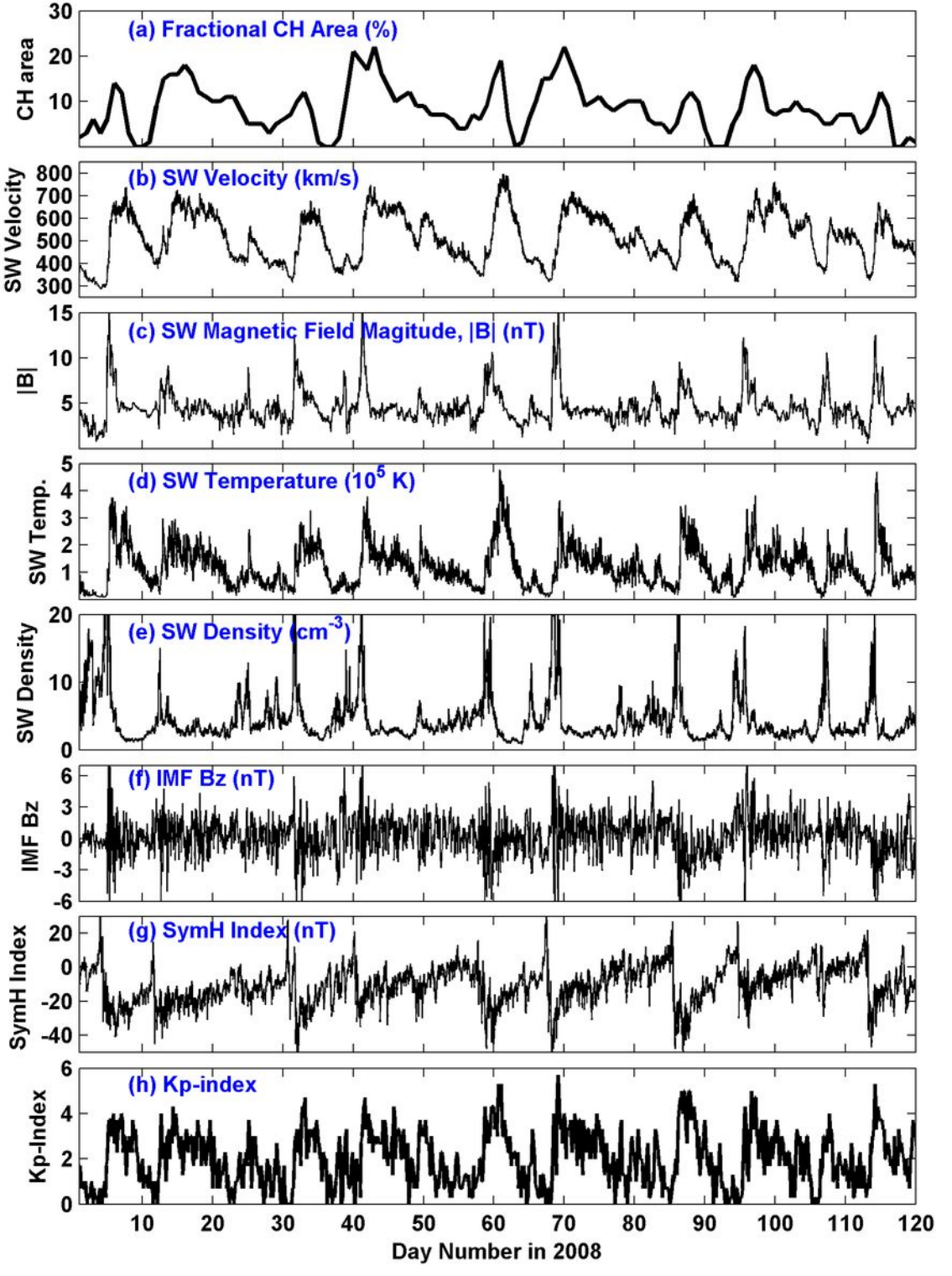
(a) Fractional CH Area (%)
CH area
30
20
10
(b) SW Velocity (km/s)
SW Velocity
800
700
600
500
400
300
(c) SW Magnetic Field Magitude, |B| (nT)
|B|
15
10
5
(d) SW Temperature (10^5 K)
SW Temp.
5
4
3
2
1
(e) SW Density (cm^{-3})
SW Density
20
10
0
(f) IMF Bz (nT)
IMF Bz
6
3
0
-3
-6
(g) SymH Index (nT)
SymH Index
20
0
-20
-40
(h) Kp-index
Kp-Index
6
4
2
0
10
20
30
40
50
60
70
80
90
100
110
120
Day Number in 2008

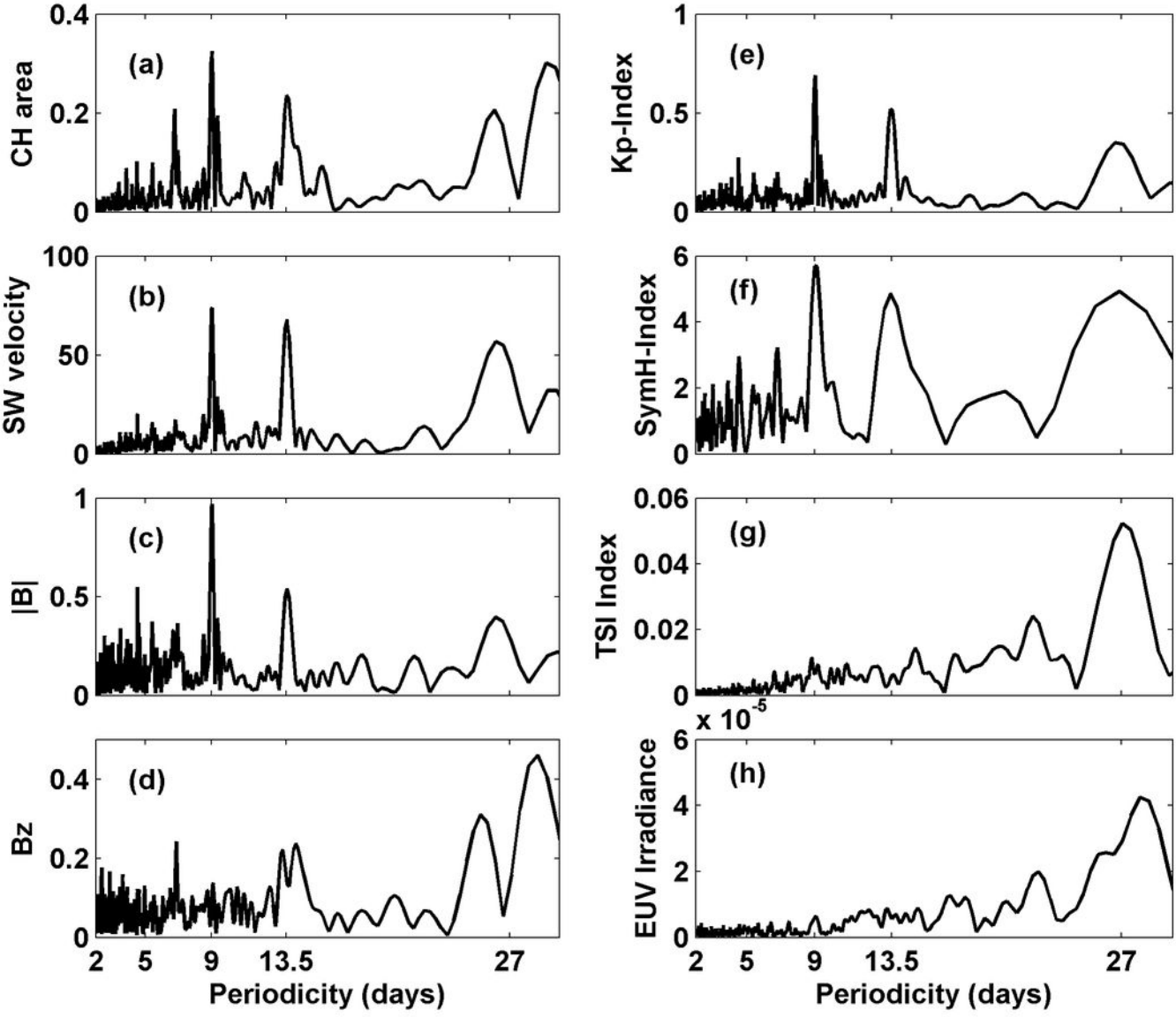
(a)
CH area
0.4
0.2
0
(b)
SW velocity
100
50
0
(c)
|B|
1
0.5
0
(d)
Bz
0.4
0.2
0
2
5
9
13.5
27
Periodicity (days)
(e)
Kp-Index
1
0.5
0
(f)
SymH-Index
6
4
2
0
(g)
TSI Index
0.06
0.04
0.02
0
x 10^-5
(h)
EUV Irradiance
6
4
2
0
2
5
9
13.5
27
Periodicity (days)

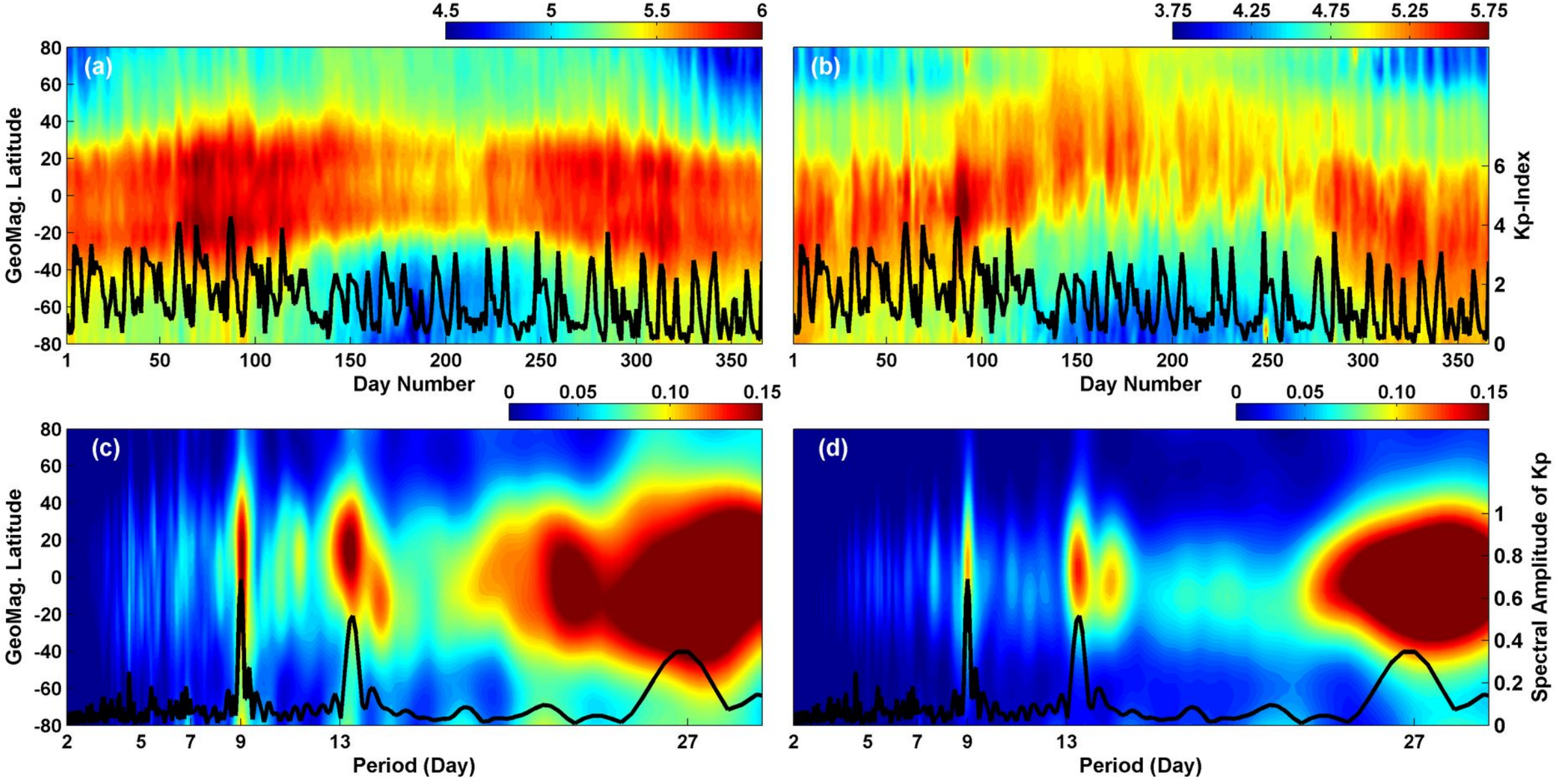
(a)
(b)
(c)
(d)
GeoMag. Latitude
Day Number
Kp-Index
Period (Day)
Spectral Amplitude of Kp
4.5
5
5.5
6
3.75
4.25
4.75
5.25
5.75
0
0.05
0.10
0.15
80
60
40
20
0
-20
-40
-60
-80
1
50
100
150
200
250
300
350
2
5
7
9
13
27
0.2
0.4
0.6
0.8
1

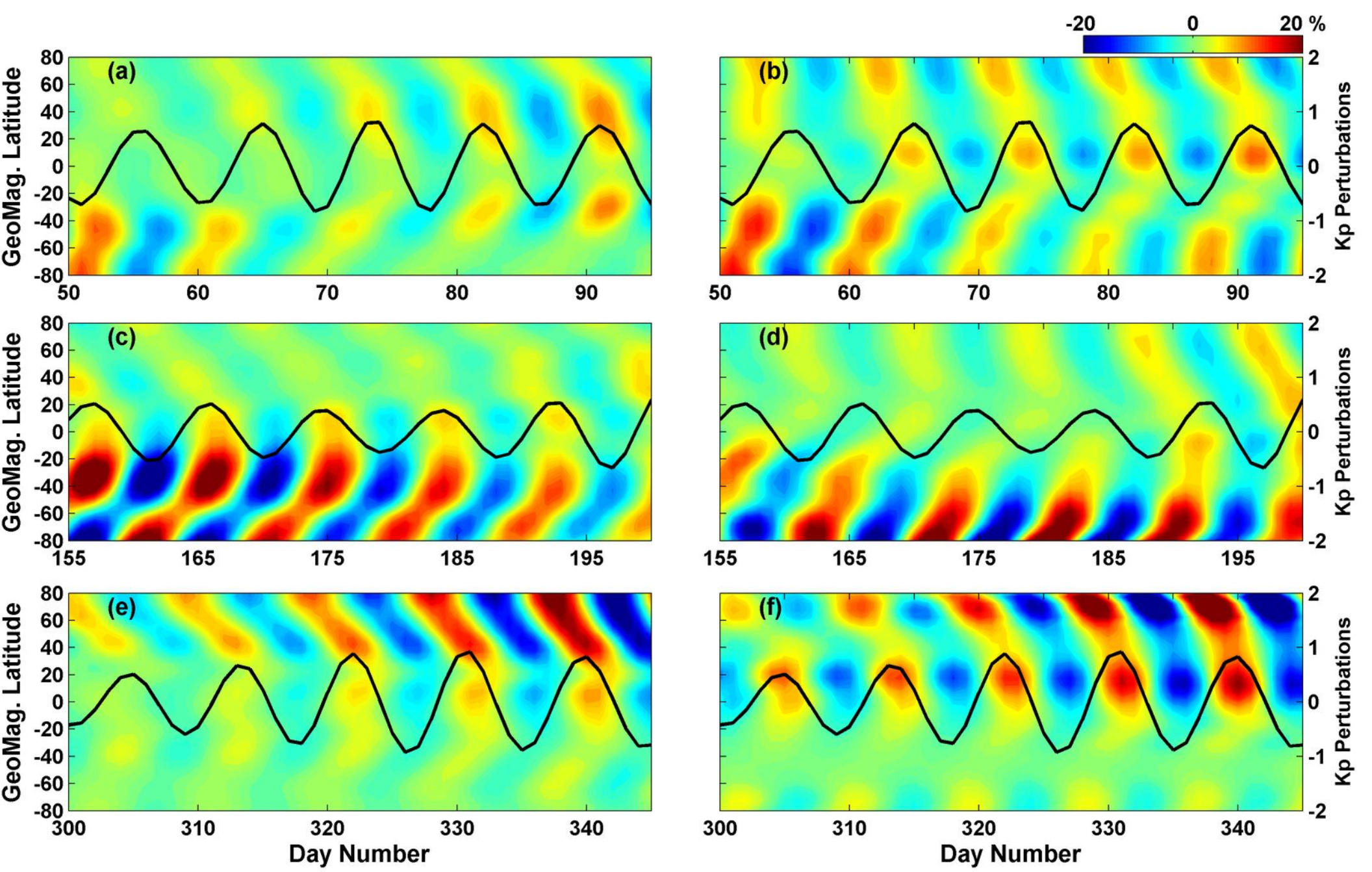
-20
0
20 %
(a)
(b)
(c)
(d)
(e)
(f)
GeoMag. Latitude
Kp Perturbations
Day Number
80
60
40
20
0
-20
-40
-60
-80
2
1
0
-1
-2
50
60
70
80
90
155
165
175
185
195
300
310
320
330
340

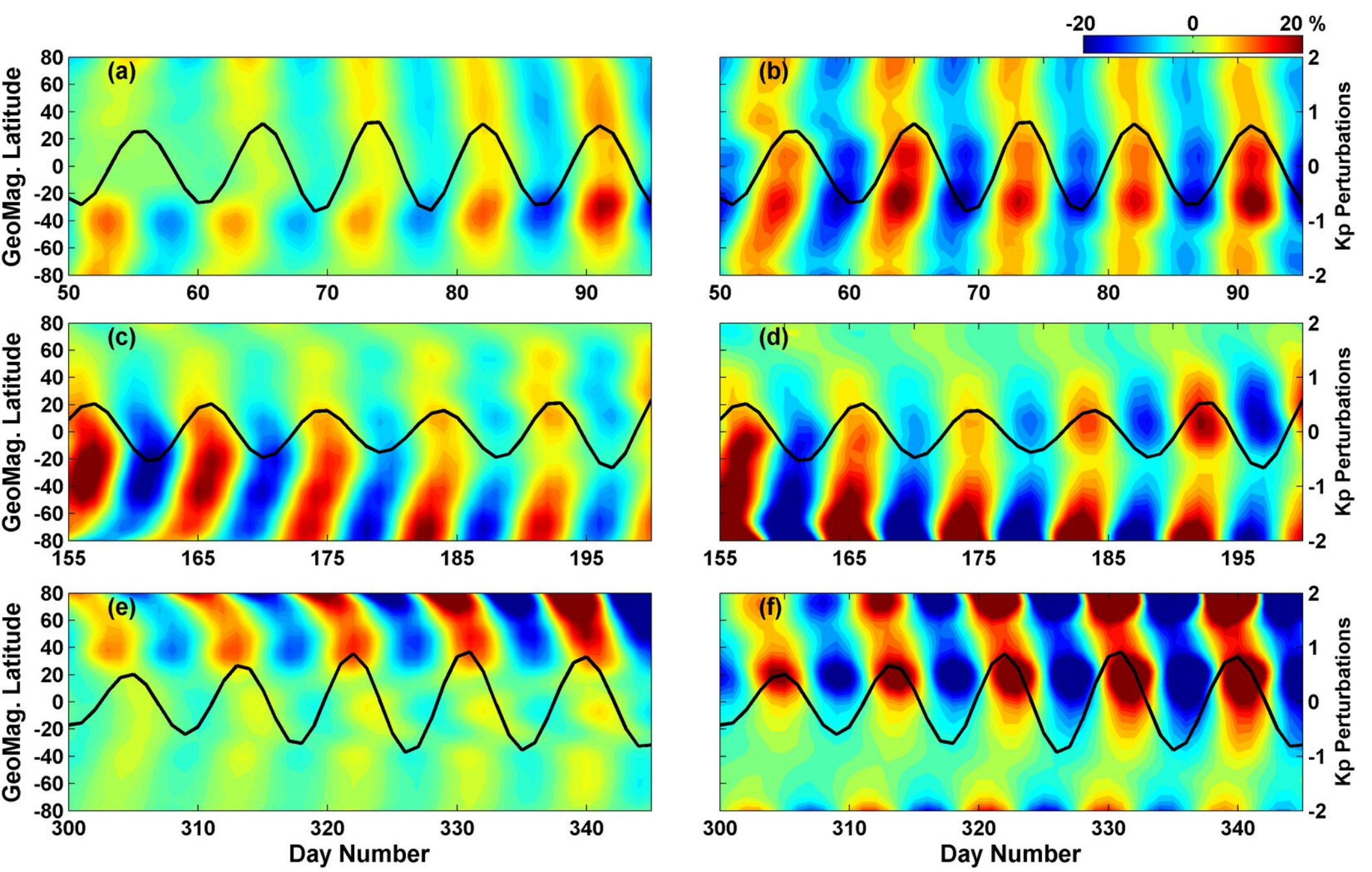
-20
0
20 %
(a)
(b)
(c)
(d)
(e)
(f)
GeoMag. Latitude
Kp Perturbations
Day Number
80
60
40
20
0
-20
-40
-60
-80
2
1
0
-1
-2
50
60
70
80
90
155
165
175
185
195
300
310
320
330
340

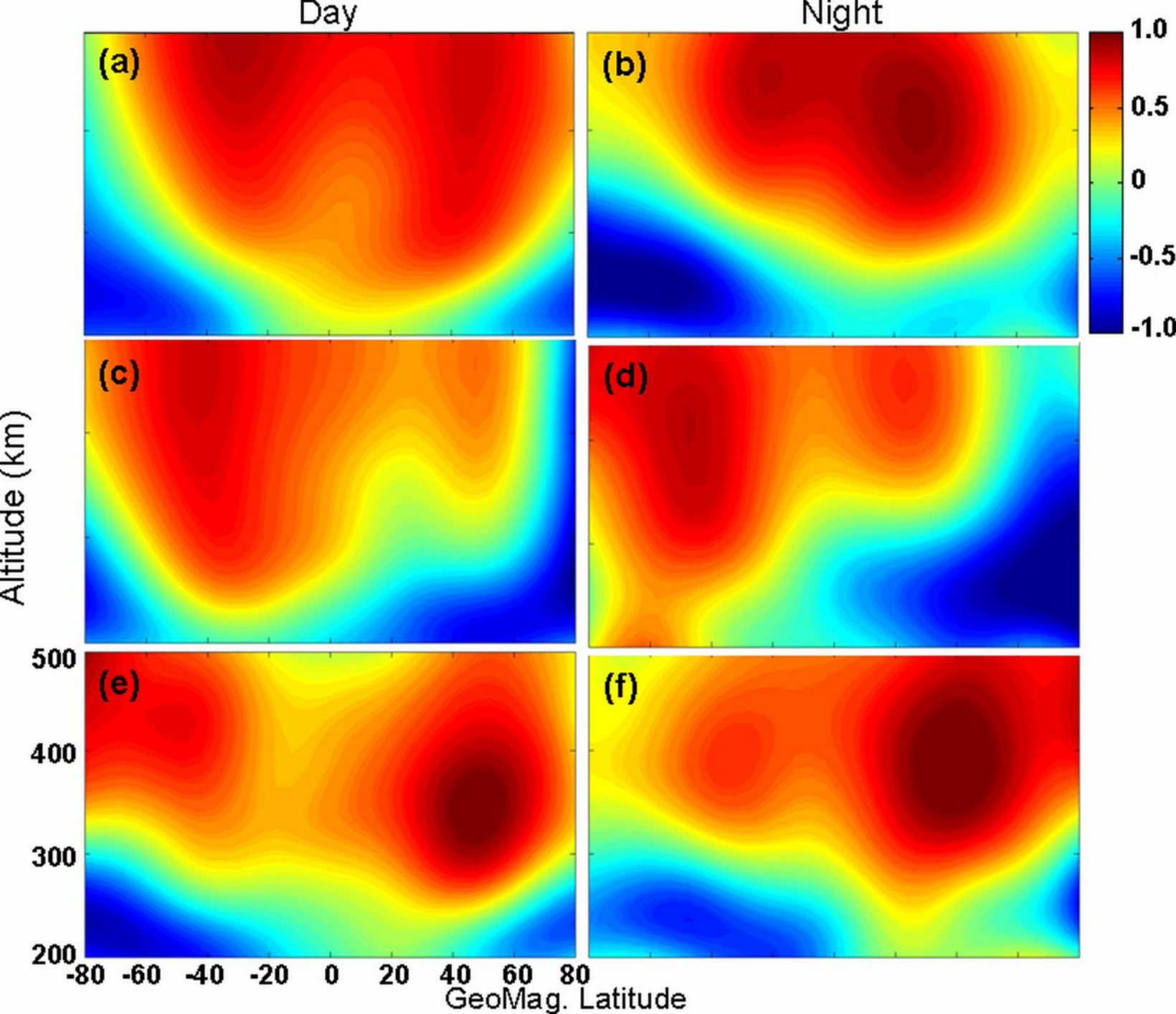
Day
Night
(a)
(b)
(c)
(d)
(e)
(f)
1.0
0.5
0
-0.5
-1.0
Altitude (km)
500
400
300
200
-80 -60 -40 -20 0 20 40 60 80
GeoMag. Latitude